

# Coherent Control of Two-Dimensional Excitons

Christopher Rogers,<sup>1,\*</sup> Dodd Gray, Jr.,<sup>1</sup> Nathan Bogdanowicz,<sup>1</sup>  
Takashi Taniguchi,<sup>2</sup> Kenji Watanabe,<sup>2</sup> and Hideo Mabuchi<sup>1,†</sup>

<sup>1</sup>*Ginzton Laboratory, Stanford University, 348 Via Pueblo, Stanford, CA 94305*

<sup>2</sup>*National Institute for Materials Science, 1-1 Namiki, Tsukuba 305-0044, Japan*

(Dated: December 29, 2021)

Electric dipole radiation can be controlled by coherent optical feedback, as has previously been studied by modulating the photonic environment for point dipoles placed both in optical cavities<sup>1–3</sup> and near metal mirrors<sup>4,5</sup>. In experiments involving fluorescent molecules<sup>4,5</sup>, trapped ions<sup>6,7</sup> and quantum dots<sup>8</sup> the point nature of the dipole, its sub-unity quantum efficiency, and decoherence rate conspire to severely limit any change in total linewidth. Here we show that the transverse coherence of exciton emission in the monolayer two-dimensional (2D) material MoSe<sub>2</sub> removes many of the fundamental physical limitations present in previous experiments. The coherent interaction between excitons and a photonic mode localized between the MoSe<sub>2</sub> and a nearby planar mirror depends interferometrically on mirror position, enabling full control over the radiative coupling rate from near-zero to 1.8 meV and a corresponding change in exciton total linewidth from 0.9 to 2.3 meV. The highly radiatively broadened exciton resonance (a ratio of up to 3 : 1 in our samples) necessary to observe this modulation is made possible by recent advances in 2D materials sample fabrication<sup>9–11</sup>. Our method of mirror translation is free of any coupling to strain or DC electric field in the monolayer, which allows a fundamental study of this photonic effect. The weak coherent driving field in our experiments yields a mean excitation occupation number of  $\sim 10^{-3}$  such that our experiments correspond to probing radiative reaction in the regime of perturbative quantum electrodynamics<sup>12</sup>. This system will serve as a testbed for exploring new excitonic physics<sup>13</sup> and quantum nonlinear optical effects<sup>14,15</sup>.

The transition metal dichalcogenides (TMDs) MoSe<sub>2</sub> and MoS<sub>2</sub> become direct band gap semiconductors when isolated in monolayer form<sup>16–18</sup>, transferring a significant fraction of the interband spectral weight to a strong and spectrally narrow excitonic resonance<sup>19,20</sup>. Coherence<sup>21</sup>, spin-valley interactions<sup>22,23</sup>, strain effects<sup>24</sup>, many-body electron physics<sup>25–27</sup> and engineered confinement<sup>28,29</sup> have all been studied using TMD excitons.

Monolayer and few-layer TMDs were first prepared by mechanical exfoliation<sup>16,17,30</sup> and were typically n-doped and inhomogeneously broadened by substrate roughness. By adding electrostatic control via a gate, the semiconductor could be made neutral<sup>26,27</sup>. Encapsulation of

TMDs in atomically flat hBN (hexagonal Boron Nitride) has enabled further improvements<sup>9–11</sup>. While some residual imperfections persist<sup>31–34</sup>, sample qualities sufficient to manifest quantum coherent effects are now achievable.

Modifying the electromagnetic environment by using a mirror to engineer the local photonic density of states can affect the radiative decay rate of a dipole<sup>1,5</sup>. In addition to those involving fluorescent molecules<sup>4,5</sup>, trapped ions<sup>6,7</sup> and quantum dots<sup>8</sup>, similar studies have been conducted with surface plasmon-polaritons<sup>35</sup> and with an acoustic gong<sup>36</sup>. For a perfect 0D dipole placed near a perfectly reflective spherical concave mirror, the radiative coupling and total linewidth could in principle be modulated from near zero to twice their vacuum values<sup>5</sup>. Experimentally, the modulation in total linewidth is much smaller due to the sub-unity quantum efficiency of real dipoles, their decoherence properties, and the use of planar mirrors (or finite numerical aperture<sup>6</sup>) for practical reasons, which partially obscure the interference effects. For a planar mirror, interference effects on the total linewidth likewise decrease rapidly with mirror-dipole distance because of the high numerical aperture of the emission pattern. However, the situation is different for excitons in 2D materials because the delocalized nature of the planar exciton leads to conservation of transverse momentum<sup>37,38</sup>, meaning that the exciton emission is angularly restricted. This opens the possibility of full manipulation of the radiative coupling even when the mirror is many wavelengths from the emitter.

The features that make this system a novel testbed for optical physics also make it attractive for engineering applications. Coupling mirror-membrane position to the frequency, linewidth and strength of a resonance is of interest for optomechanics. For nonlinear and quantum optics, controllably reducing the intrinsic linewidth would greatly enhance nonlinearities<sup>15</sup>. High quality TMDs grown by chemical vapor deposition<sup>39,40</sup> and then laser annealed to improve sample quality<sup>41</sup> offer a path towards scalable quantum engineering applications.

We report the effect of varying the distance between the monolayer semiconductor MoSe<sub>2</sub> and a metal mirror on the MoSe<sub>2</sub> exciton resonance ( $X_0$ ). A low-finesse photonic mode is formed between the mirror and MoSe<sub>2</sub>, and light coupling out of this cavity interferes with light directly emitted by the exciton. As the mirror is translated, the interference condition at the MoSe<sub>2</sub> varies between destructive and constructive, strongly modifying the reflection of the device. The magnitude of the reflection at  $X_0$  can vary from near zero to near unity, and the

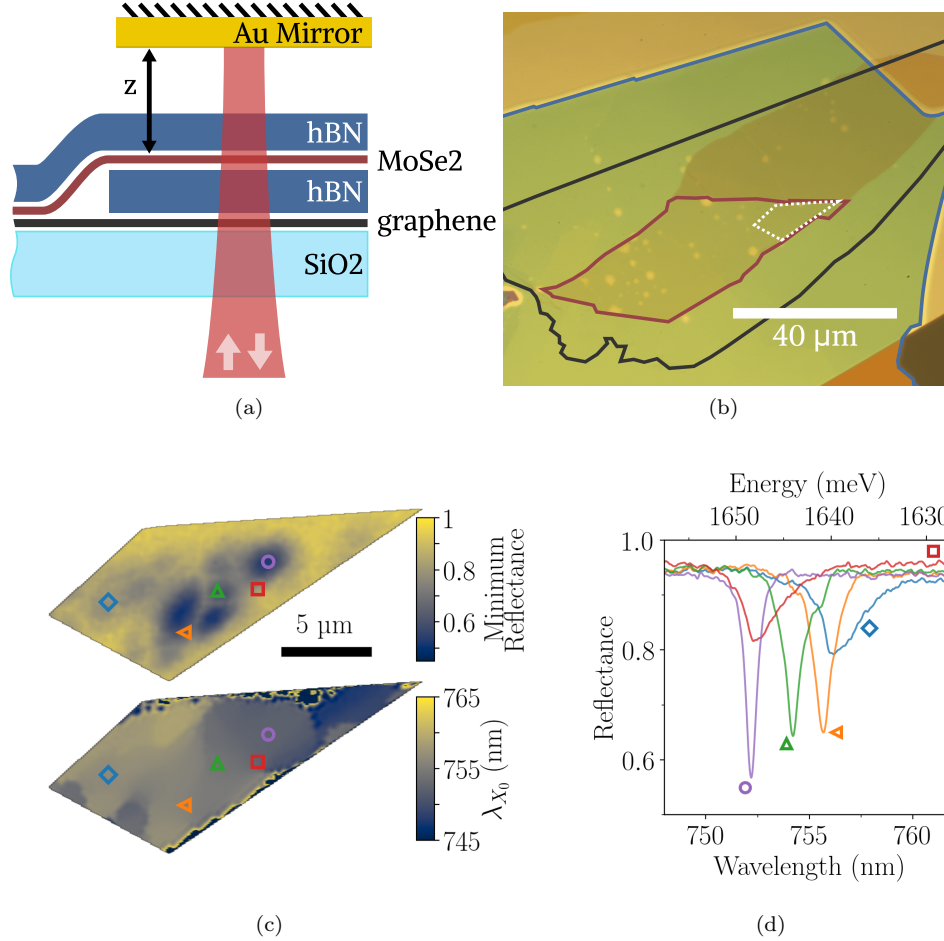


FIG. 1. **Sample Characterization.** (a) A schematic of the heterostructure device. The Au mirror is mounted on a mechanical actuator so that  $z$  can be varied. (b) A microscope image of the sample. The monolayer MoSe<sub>2</sub> region is outlined in burgundy. A few-layer graphene flake outlined in black on the bottom of the stack electrostatically isolates the MoSe<sub>2</sub> from the SiO<sub>2</sub> substrate. The bottom hBN is outlined in blue. (c) Spatial maps of the maximum dip in reflection at  $X_0$ , and its center wavelength  $\lambda_{X_0}$  from a region of the sample corresponding to the area outlined with dashed white lines in (b). (d) Selected reflection spectra corresponding to the marked positions in (c). These spectra were collected at 4 K with the mirror positioned slightly away from maximum destructive interference.

absorption varies in a complementary way. This interference condition also affects the radiative coupling of  $X_0$  to the environment, and at maximal destructive interference the coupling can be almost entirely suppressed, in theory limited only by mirror losses. Conversely, at maximal constructive interference this coupling is twice its vacuum value. Since  $X_0$  is primarily radiatively broadened, this modulation of the radiative coupling induces a similar effect on the total linewidth.

In the experiment we fabricate heterostructures of MoSe<sub>2</sub> encapsulated in hBN, and then transfer these stacks onto fused silica substrates<sup>42,43</sup>. A microscope image of the sample used for the data presented in this paper is shown in Fig. 1b, and a schematic of the experiment is shown in Fig. 1a. Experiments are conducted within an optical cryostat at 4 K. A gold mirror on a mechanical actuator is placed in close proximity to the MoSe<sub>2</sub> heterostructure. The mirror is translated along

the optical axis, and at selected  $z$  positions reflectance measurements are made using a grating spectrometer. Note that  $z$  is the *optical* path length between the mirror and the MoSe<sub>2</sub>. This method of mirror translation isolates the effect of coherent electromagnetic feedback since it is entirely free of coupling to strain or electric field in the TMD. More detail on the samples and the experiment can be found in the methods sections IA and IB. Because we excite with  $\sim 15$  nW of continuous-wave optical power with a bandwidth of 300 nm the photon rate at the sample is  $\sim 60$  GHz, and considering only optical power resonant with  $X_0$  the rate is  $\sim 0.4$  GHz. Taking into account the exciton decay rate of  $\sim 2$  meV  $\approx 480$  GHz, the excitation occupation number during the measurement is very low,  $\sim 10^{-3}$ .

Maps of the magnitude of the dip in reflectance at  $X_0$  and its center frequency/wavelength ( $\omega_{X_0}$ ,  $\lambda_{X_0}$ ) are shown in Fig. 1c. The mirror is near but not at maxi-

imum destructive interference. As observed by others<sup>9,10</sup>, there is inhomogeneity on a few-micron scale in both  $\lambda_{X_0}$  and the magnitude of the reflection. Nonetheless, some areas of the sample are radiatively broadened. In Fig. 1d, spots are selected to show both a range of sample quality and  $\lambda_{X_0}$ .

A heat map of the reflectance as a function of mirror position is shown in Fig. 2a, along with selected line cuts of the same data in Fig. 2c. The  $X_0$  resonance appears as a dip (the central bright band) that varies in magnitude, width and center frequency as the mirror is translated across a full fringe. We define  $z_d$  and  $z_c$  as the mirror positions for maximal destructive and constructive interference respectively, as in Fig. 2b. When the reflection from the mirror interferes destructively with that from the MoSe<sub>2</sub>, the radiative coupling of  $X_0$  becomes very small and the dip disappears below the noise floor ( $z_{d,1}$  and  $z_{d,2}$  in Fig. 2a). Surprisingly, the minimum reflection over  $z$  does not occur at  $z_c$ , but rather occurs at each of two mirror positions on either side of  $z_c$ . At these two reflection minima ( $z_{m,1} = 815$  nm and  $z_{m,2} = 1020$  nm) the reflectance is  $\sim 8\%$ , while in between it reaches 45% at  $z_c$ .

This surprising effect is due to an interplay between the radiative coupling rate ( $\gamma_r$ ) and non-radiative coupling rate ( $\gamma_{nr}$ ). At  $z_c$ , the exciton is primarily radiatively broadened and  $\gamma_r$  is larger than  $\gamma_{nr} + \gamma_{ib,eff}$ , where  $\gamma_{ib,eff}$  is the effective contribution to the total linewidth from a Gaussian inhomogeneous broadening  $\gamma_{ib}$ . We define  $\gamma_{tot} = \gamma_r + \gamma_{nr} + \gamma_{ib,eff}$  as the total linewidth. In an ideal material ( $\gamma_r \gg \gamma_{nr}, \gamma_{ib,eff}$ ) the reflectance would approach unity here. However, in our real sample  $\gamma_{nr}$  and  $\gamma_{ib,eff}$  reduce the reflectance feature at  $z_c$  to 45%. When the mirror is moved in either direction from  $z_c$ ,  $\gamma_r$  and  $\gamma_r/\gamma_{nr}$  are reduced so that the exciton begins to absorb more light, causing the reflectance feature to deepen and eventually reach its minimum value at  $z_{m,1/2}$ . It also begins to spectrally narrow, since the contribution of  $\gamma_r$  to the total linewidth  $\gamma_{tot}$  is reduced. As the mirror is moved even farther away from  $z_c$  past  $z_{m,1/2}$ ,  $\gamma_r$  continues to decrease and the  $X_0$  feature shrinks while spectrally narrowing until it eventually disappears.

Note that the center frequency  $\omega_{X_0}$  of the dip changes with mirror position as well. When the light reflected from the mirror is exactly in- or out-of-phase with that back-emitted from the MoSe<sub>2</sub>, the dip is at its ‘vacuum’ frequency ( $\omega_0$ ), and  $\omega_{X_0} = \omega_0$ . However, away from either of these positions dispersion over the  $X_0$  resonance causes a spectrally asymmetric interference condition, which shifts the effective line center  $\omega_{X_0}$ .

Plots of the modeled reflectance are shown in Figs. 2a and 2c. We model the TMD exciton using a Lorentzian susceptibility, shown in Eq. 1, which accounts for radiative broadening  $\gamma_r$  and non-radiative broadening  $\gamma_{nr}$ <sup>10,44</sup>. The reflectance is calculated for the full heterostructure and mirror using a transfer matrix method<sup>45</sup> including the effect of inhomogeneous broadening  $\gamma_{ib}$ . Selected line cuts were simultaneously fit to the model to find global

values for  $\gamma_r$ ,  $\gamma_{nr}$ ,  $\gamma_{ib}$  and  $\omega_{X_0}$ . See the methods section IC for more details. Both qualitatively and quantitatively, the model matches closely with the experimental data. One slight difference is that the deepest reflectance feature obtained over  $z$  is smaller in the experiment (8%) than the model (18%), which is likely due to a combination of pure dephasing (which is not included in the model), spectrally structured inhomogeneous broadening, mode-mismatch between the interfering reflected beams, and diffraction effects. We attribute the slight discrepancy (distortion along  $z$ ) between the model and experiment on the left in Fig. 2a to small imperfections in the  $z$  calibration of the data.

From both the experimental data and the model we extract full-width-half-max (FWHM) linewidths, which are shown in Fig. 3a. As a function of mirror position, the linewidth  $\gamma_{tot}$  varies from  $\sim 0.9$  meV near  $z_d$  to  $\sim 2.3$  meV at  $z_c$  for a total modulation of  $\sim 2.5\times$ , while in the model it varies from 0.9 to 2.4 meV, or  $\sim 2.6\times$ . This modulation can also be clearly seen in Fig. 2d. The change in  $\gamma_r$  of the  $X_0$  resonance is the primary cause of the change in  $\gamma_{tot}$ , and the values of  $\gamma_r$  extracted from the model vary from near zero at  $z_d$  to 1.8 meV (440 GHz) at  $z_c$ . Near  $z_d$ ,  $\gamma_{tot}$  is dominated by the contribution of  $\gamma_{nr}$  and  $\gamma_{ib,eff}$  while at  $z_c$  radiative coupling dominates, with a ratio of  $\gamma_r/(\gamma_{nr} + \gamma_{ib,eff}) \sim 3$ . Modeled and experimental values for  $\omega_{X_0}$  and the minimum reflectance shown in Figs. 3b and 3c agree as well. The line shift of  $\sim 1$  meV (240 GHz) is significant relative to  $\gamma_{tot}$ .

Lastly, in Fig. 3d we compare our data to a simplified model of both a 2D dipole and a point dipole. The 2D case highlights that the transverse coherence and delocalized nature of the exciton causes light emission into specific modes rather than the full numerical aperture. We define the coherent quantum efficiency in vacuum  $\eta_0 = \gamma_r/\gamma_{tot}$ , which differs from the incoherent quantum efficiency  $\gamma_r/(\gamma_r + \gamma_{nr})$ . For our purpose, coherent quantum efficiency is the relevant quantity because the linewidth modulation effect depends on the coherent interference of emitted waves. Using models described in methods section ID, we show that for an ideal 2D dipole ( $\eta_0 = 1$ ) and a perfect planar mirror, the linewidth can be fully modulated even when the mirror is far from the dipole. This is not true in the 0D dipole case, because integrating emission over the full numerical aperture obscures the interference effect as  $z$  increases. Also shown is a plot for  $\eta_0 = 0.45$  chosen to match the superimposed experimental data. Note that the peak ratio  $\gamma_r/(\gamma_{nr} + \gamma_{ib,eff}) \sim 3$  extracted from the reflectance model does not match that of  $\gamma_r/(\gamma_{nr} + \gamma_{ib,eff}) \sim 1.8$  we expect for  $\eta_0 = 0.45$  from this simplified model. This discrepancy is primarily due to  $\gamma_{ib,eff}$  varying with  $z$  so as to partially counteract the change in  $\gamma_r$ , as seen in Fig. 3a. Because the intrinsically Lorentzian exciton feature is convolved with a Gaussian inhomogeneous broadening of width  $\gamma_{ib}$  to form a Voigt profile, the effective inhomogeneous broadening  $\gamma_{ib,eff}$  is larger when the total linewidth  $\gamma_{tot}$  is small<sup>46,47</sup>. Regardless, the amplitude

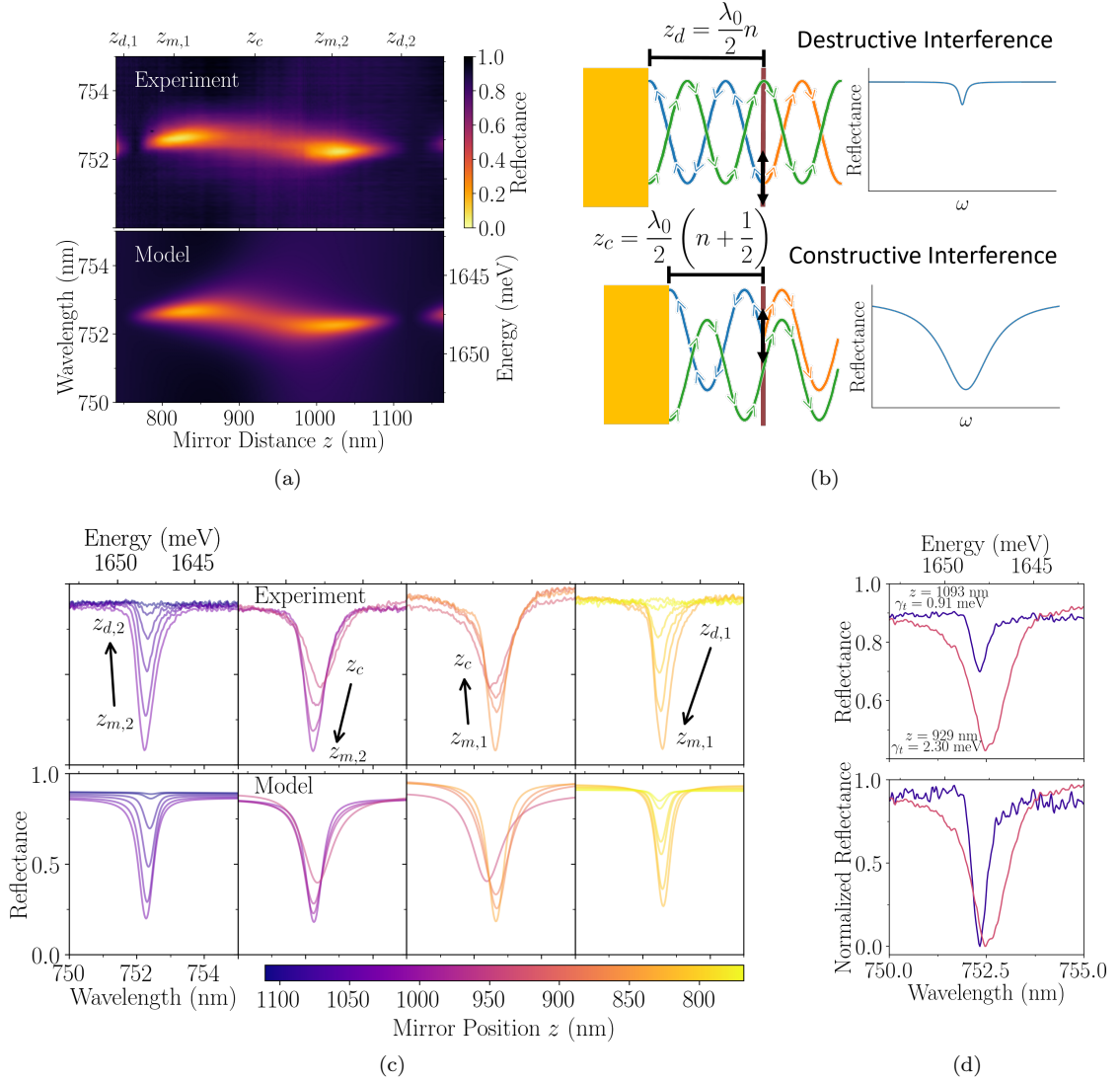


**FIG. 2. Experimental and Modeled Reflectance.** (a) Measured and modeled reflectance spectra near the  $X_0$  resonance as  $z$  is varied over a full fringe. Measurements at 4 K. Note that this data comes from near the region marked with a purple circle in Fig. 1c. (b) A schematic representation of the effect of mirror position  $z$  on the exciton resonance. The black double-headed arrow represents the exciton electric dipole, and the blue and orange curves represent the electric field emitted towards and away from the mirror, respectively. The electric field reflected by the mirror is represented in green. To the right of the monolayer the fields interfere either constructively or destructively depending on mirror position. The corresponding schematic plots represent the modulation of amplitude and linewidth of the  $X_0$  feature. The  $z_d$  and  $z_c$  values shown respectively for the destructive and constructive interference cases respectively, assume a perfect mirror with zero skin-depth. For simplicity, multiple reflections and the full heterostructure have been omitted. (c) Selected line cuts of the measured and modeled reflectance in the spectral region of  $X_0$ . The black arrows indicate increasing  $z$ . (d) Measured reflectance, both absolute and normalized, at two  $z$  positions highlighting the modulation of total linewidth.

and phase of the experimental  $\gamma_{\text{tot}}$  values highlight that no 0D dipole in front of a flat mirror (even with a perfect mirror and  $\eta_0 = 1$ ) could produce the behavior seen in the experiments.

We have demonstrated coherent control over an exciton resonance by positioning a mirror in close proximity to the monolayer semiconductor MoSe<sub>2</sub>, showing near complete modulation of the reflection at  $X_0$ . The concurrent change in radiative coupling rate induces a

change in total linewidth of  $\sim 2.4\times$ , demonstrating the dominant role of radiative coupling for excitons in monolayer MoSe<sub>2</sub> and serving as an important verification of theoretical models used to describe excitonic physics in TMD materials. For engineering applications, the modulation of the  $X_0$  resonance could greatly enhance optomechanical couplings, while the effective enhancement of nonlinearities<sup>15</sup> is useful for nonlinear optics and quantum optics. Our strain free and DC electric



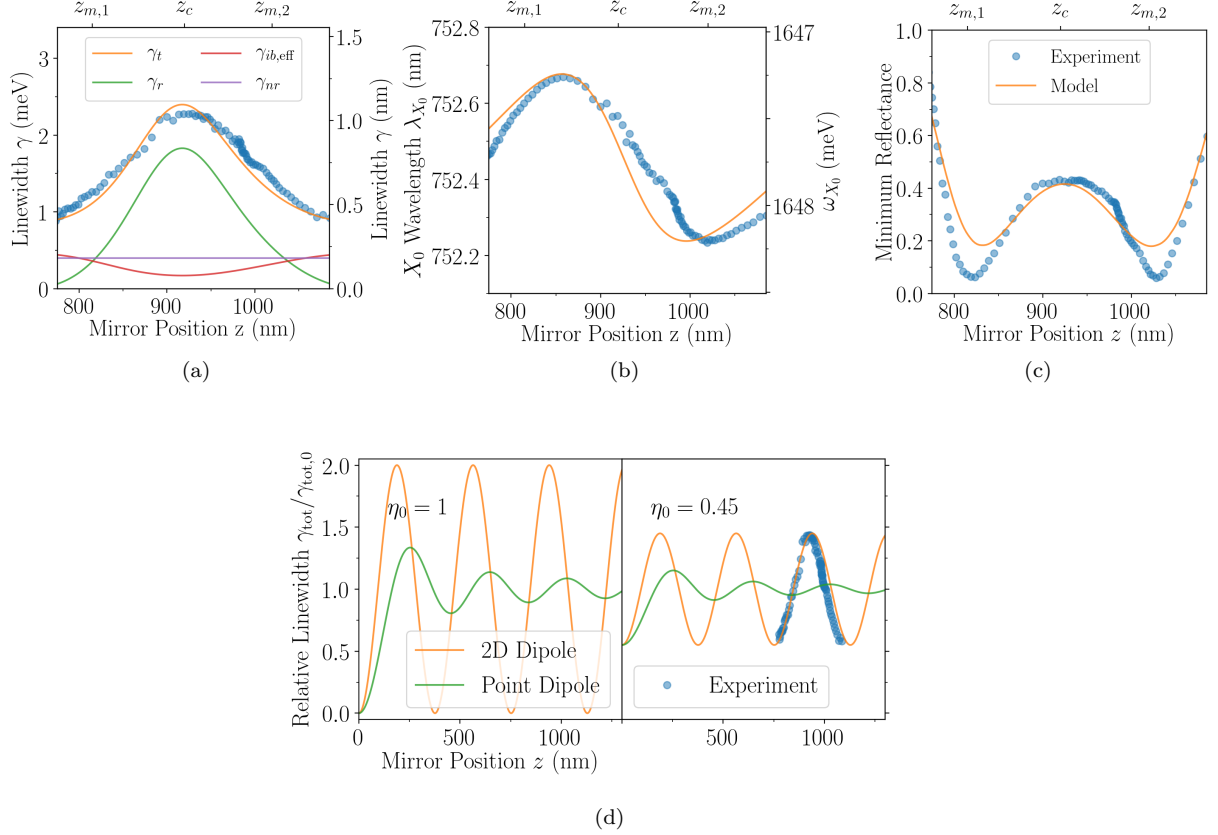


FIG. 3. **Extracted and Modeled Linewidths.** (a) The FWHM linewidth  $\gamma_{tot}$  both from the model and extracted from the experimental data. Note that we cannot extract linewidth data over the full range of the experimental data, since near  $z_d$  the  $X_0$  resonance is almost completely extinguished. Also shown are  $\gamma_r$ ,  $\gamma_{nr}$  and  $\gamma_{ib,eff}$  from the model. (b) Center frequency  $\omega_{X_0}$  for both model and experiment. (c) Minimum reflectance for both model and experiment. (d) Simplified models of the total linewidth modulation for both a point and 2D dipole, assuming a perfect mirror with zero skin depth. On the left is shown the ideal case with coherent quantum efficiency in vacuum  $\eta_0 = 1$ , and on the right with  $\eta_0 = 0.45$  alongside the experimental data.

field free method of mirror positioning has allowed us to study the underlying photonic interference effect present in the system, and the unprecedented control over the radiative coupling of an excitonic resonance paves the way for many future experiments.

*Note:* During preparation of this manuscript we became aware of a preprint presenting similar work by You Zhou, et. al.<sup>48</sup>.

## I. METHODS

### A. Sample Preparation

We fabricate heterostructures like the one shown in Figs. 1a and 1b using a dry pickup transfer technique<sup>42,43</sup>. First, hBN, MoSe<sub>2</sub> and graphite are mechanically exfoliated<sup>16,17,30</sup> onto 300 nm SiO<sub>2</sub> on Si substrates. The substrates are then observed under an optical microscope to identify suitable flakes. Polycarbon-

ate (PC) ‘stamps’ are made by affixing a thin PC film to a piece of polydimethylsiloxane (PDMS) on a glass slide. This stamp is then used to sequentially pick up the mechanically exfoliated flakes by bringing the stamp slowly into contact with a flake on the exfoliation substrate. In our case, we first pick up the ‘top’ hBN, then the monolayer MoSe<sub>2</sub>, then the ‘bottom’ hBN and finally the few-layer graphene flake. This stack (including the PC film) is transferred to a glass substrate. The PC is removed by dissolution in chloroform. Note that the MoSe<sub>2</sub> protrudes from the bottom hBN so that it contacts the few-layer graphene flake, shorting the two to each other. This helps to electrostatically isolate the MoSe<sub>2</sub> from the substrate. More details on sample preparation are given in the supplemental material.

The mirrors are prepared by taking a small glass substrate ( $\sim 1$  mm x 1 mm in lateral dimensions) and affixing it to a larger carrier substrate. This is then coated in 120 nm of gold, with a 3 nm titanium adhesion layer.

## B. Experimental Setup

The experiment is conducted in an optical cryostat (Montana Instruments Nanoscale Workstation). All measurements were conducted at a nominal temperature of 4 K and a pressure of  $1 \cdot 10^{-7}$  Torr. The sample is attached to a fixed mount. A gold mirror is mounted on a slip-stick piezo mirror mount (Janssen Precision Engineering) and brought close to the sample. The slip-stick piezo mirror mount is used to translate the mirror relative to the sample. A microscope objective (20 $\times$ , 0.4 numerical aperture, Olympus MSPLAN) inside the cryostat was used to focus the beam onto the sample.

Light from either a lamp (Thorlabs SLS201) or a supercontinuum laser (NKT Photonics SuperK) is focused into a single mode optical fiber. This light is coupled into a home-built confocal microscope setup, which focuses the beam onto the sample. The collected reflected light is then sent to a home-built grating spectrometer for measurement. In order to translate the focus of the beam in three dimensions at the sample, the confocal microscope has a double 4f system. One tip-tilt mirror in the second 4f section translates the beam in the transverse plane, while a lens in the first 4f system is translated along the optical axis to move the beam focus along the optical axis. More details of the experimental setup can be found in the supplemental information. Each spectrum is normalized to a spectrum taken at a flake-free area on the substrate. Measurements were automated using the python instrument control package Instrumental<sup>49</sup>, available on GitHub at <https://github.com/mabuchilab/Instrumental>.

## C. Reflectance Model

For simplicity we use a classical model of stack reflectivity based on a Lorentzian susceptibility for the MoSe<sub>2</sub> exciton, taking into account radiative broadening in vacuum  $\gamma_{r,0}$  and non-radiative broadening  $\gamma_{nr}$ <sup>10,44</sup>:

$$\chi_{\text{exc}} = -\frac{c}{\omega_0 d} \frac{\gamma_{r,0}}{\omega - \omega_0 + \frac{i\gamma_{nr}}{2}} \quad (1)$$

where  $\omega_0$  is the exciton center frequency,  $\omega$  is the optical frequency,  $c$  is the speed of light, and  $d$  is the MoSe<sub>2</sub> thickness. The index of refraction of the MoSe<sub>2</sub> is then:

$$n_{\text{exc}} = \sqrt{n_0^2 + \chi_{\text{exc}}} \quad (2)$$

where  $n_0$  is the background index in the MoSe<sub>2</sub>. Reflectance from the full stack  $R_{\omega_0}(\omega)$  including the mirror is calculated using a transfer-matrix-method to obtain Fresnel coefficients<sup>45</sup>. Inhomogeneous broadening effects are included with a characteristic width of  $\gamma_{ib}$ . To obtain

the reflectance  $R(\omega)$  including inhomogeneous broadening,  $R_{\omega_0}(\omega)$  is calculated for a range of exciton center frequencies and combined by weighting with a Gaussian of width  $\gamma_{ib}$ :

$$R(\omega) = \frac{1}{\sqrt{2\pi}\gamma_{ib}} \int R_{\omega'_0}(\omega) e^{-(\omega_0 - \omega'_0)^2 / 2\gamma_{ib}^2} d\omega'_0 \quad (3)$$

This assumes that the inhomogeneously broadened excitons emit incoherently, so that interference effects average out.

For fitting purposes, data from several line cuts at characteristic mirror positions were selected. The model was fit to all line cuts simultaneously, resulting in the following values for the free parameters:  $\omega_0 = 1647.72$  meV,  $\gamma_{r,0} = 1.09$  meV,  $\gamma_{nr} = 0.40$  meV and  $\gamma_{ib} = 0.26$  meV. The mirror distance  $z$  was also extracted from the spectra by fitting interference fringes at wavelengths far from  $\omega_0$ . See the supplemental information for more details of both fitting procedures, and the values for the static parameters used in the reflectance model.

To extract the model parameters in Fig. 3a we first extract the total FWHM linewidth of the  $X_0$  feature from the reflectance model as a function of mirror position  $z$ . Assuming a Voigt line shape<sup>46,47</sup> we can extract the intrinsic Lorentzian linewidth ( $\gamma_r + \gamma_{nr}$ ) because the intrinsic Gaussian linewidth ( $\gamma_{ib}$ ) is known directly from the model. This also yields the effective contribution to the linewidth of inhomogeneous broadening ( $\gamma_{ib,\text{eff}}$ ) as the difference between the total linewidth and the intrinsic Lorentzian linewidth. We can then trivially extract  $\gamma_r$  from the intrinsic Lorentzian linewidth because  $\gamma_{nr}$  is known.

## D. Simplified Linewidth Model

Simplified models for the linewidth modulation of 0D and 2D dipoles parallel to a perfect planar mirror were derived. The normalized total linewidth as a function of distance from the mirror is<sup>5</sup>:

$$\frac{\gamma_{\text{tot}}(x)}{\gamma_{\text{tot},0}} = 1 + \eta_0 \left[ \frac{3 \sin x}{2x^3} - \frac{3 \cos x}{2x^2} - \frac{3 \sin x}{2x} \right] \quad (4)$$

where  $\gamma_{\text{tot}}(x)$  is the total linewidth at normalized mirror position  $x = \frac{4\pi z}{\lambda_0}$ ,  $\gamma_{\text{tot},0}$  is the total linewidth in vacuum and  $\lambda_0$  is the wavelength in vacuum. Following a similar procedure an equation for a 2D material was derived:

$$\frac{\gamma_{\text{tot}}(x)}{\gamma_{\text{tot},0}} = 1 - \eta_0 \cos x \quad (5)$$

See the supplemental information for details of the derivation.

- \* [cmrogers@stanford.edu](mailto:cmrogers@stanford.edu)  
† [hmabuchi@stanford.edu](mailto:hmabuchi@stanford.edu)
- <sup>1</sup> E. M. Purcell, H. C. Torrey, and R. V. Pound, “Resonance Absorption by Nuclear Magnetic Moments in a Solid,” *Phys. Rev.* **69**, 37–38 (1946).
  - <sup>2</sup> D. J. Heinzen, J. J. Childs, J. E. Thomas, and M. S. Feld, “Enhanced and inhibited visible spontaneous emission by atoms in a confocal resonator,” *Phys. Rev. Lett.* **58**, 1320–1323 (1987).
  - <sup>3</sup> A. M. Vredenberg, N. E. J. Hunt, E. F. Schubert, D. C. Jacobson, J. M. Poate, and G. J. Zydzik, “Controlled atomic spontaneous emission from  $\text{Er}^{3+}$  in a transparent Si/SiO<sub>2</sub> microcavity,” *Phys. Rev. Lett.* **71**, 517–520 (1993).
  - <sup>4</sup> K. H. Drexhage, H. Kuhn, and F. P. Schäfer, “Variation of the Fluorescence Decay Time of a Molecule in Front of a Mirror,” *Berichte der Bunsengesellschaft für physikalische Chemie* **72**, 329–329 (1968).
  - <sup>5</sup> K. H. Drexhage, “Influence of a dielectric interface on fluorescence decay time,” *Journal of Luminescence* **1-2**, 693–701 (1970).
  - <sup>6</sup> J. Eschner, Ch Raab, F. Schmidt-Kaler, and R. Blatt, “Light interference from single atoms and their mirror images,” *Nature* **413**, 495 EP – (2001).
  - <sup>7</sup> M. A. Wilson, P. Bushev, J. Eschner, F. Schmidt-Kaler, C. Becher, R. Blatt, and U. Dörner, “Vacuum-Field Level Shifts in a Single Trapped Ion Mediated by a Single Distant Mirror,” *Phys. Rev. Lett.* **91**, 213602 (2003).
  - <sup>8</sup> S. Stobbe, J. Johansen, P. T. Kristensen, J. M. Hvam, and P. Lodahl, “Frequency dependence of the radiative decay rate of excitons in self-assembled quantum dots: Experiment and theory,” *Phys. Rev. B* **80**, 155307 (2009).
  - <sup>9</sup> F. Cadiz, E. Courtade, C. Robert, G. Wang, Y. Shen, H. Cai, T. Taniguchi, K. Watanabe, H. Carrere, D. Lagarde, M. Manca, T. Amand, P. Renucci, S. Tongay, X. Marie, and B. Urbaszek, “Excitonic Linewidth Approaching the Homogeneous Limit in MoS<sub>2</sub>-Based van der Waals Heterostructures,” *Phys. Rev. X* **7**, 021026 (2017).
  - <sup>10</sup> Giovanni Scuri, You Zhou, Alexander A. High, Dominik S. Wild, Chi Shu, Kristiaan De Greve, Luis A. Jauregui, Takashi Taniguchi, Kenji Watanabe, Philip Kim, Mikhail D. Lukin, and Hongkun Park, “Large Excitonic Reflectivity of Monolayer MoSe<sub>2</sub> Encapsulated in Hexagonal Boron Nitride,” *Phys. Rev. Lett.* **120**, 037402 (2018).
  - <sup>11</sup> Patrick Back, Sina Zeytinoglu, Aroosa Ijaz, Martin Kroner, and Atac Imamoglu, “Realization of an Electrically Tunable Narrow-Bandwidth Atomically Thin Mirror Using Monolayer MoSe<sub>2</sub>,” *Phys. Rev. Lett.* **120**, 037401 (2018).
  - <sup>12</sup> D. Meschede, W. Jhe, and E. A. Hinds, “Radiative properties of atoms near a conducting plane: An old problem in a new light,” *Phys. Rev. A* **41**, 1587–1596 (1990).
  - <sup>13</sup> Tim Byrnes, Na Young Kim, and Yoshihisa Yamamoto, “Exciton-polariton condensates,” *Nature Physics* **10**, 803 EP – (2014), review Article.
  - <sup>14</sup> Sina Zeytinoglu, Charlaïne Roth, Sebastian Huber, and Atac Imamoglu, “Atomically thin semiconductors as nonlinear mirrors,” *Phys. Rev. A* **96**, 031801 (2017).
  - <sup>15</sup> Dominik S. Wild, Ephraim Shahmoon, Susanne F. Yelin, and Mikhail D. Lukin, “Quantum Nonlinear Optics in Atomically Thin Materials,” *Phys. Rev. Lett.* **121**, 123606 (2018).
  - <sup>16</sup> Kin Fai Mak, Changgu Lee, James Hone, Jie Shan, and Tony F. Heinz, “Atomically Thin MoS<sub>2</sub>: A New Direct-Gap Semiconductor,” *Phys. Rev. Lett.* **105**, 136805 (2010).
  - <sup>17</sup> Andrea Splendiani, Liang Sun, Yuanbo Zhang, Tianshu Li, Jonghwan Kim, Chi-Yung Chim, Giulia Galli, and Feng Wang, “Emerging Photoluminescence in Monolayer MoS<sub>2</sub>,” *Nano Letters* **10**, 1271–1275 (2010).
  - <sup>18</sup> Yi Zhang, Tay-Rong Chang, Bo Zhou, Yong-Tao Cui, Hao Yan, Zhongkai Liu, Felix Schmitt, James Lee, Rob Moore, Yulin Chen, Hsin Lin, Horng-Tay Jeng, Sung-Kwan Mo, Zahid Hussain, Arun Bansil, and Zhi-Xun Shen, “Direct observation of the transition from indirect to direct bandgap in atomically thin epitaxial MoSe<sub>2</sub>,” *Nature Nanotechnology* **9**, 111 EP – (2013).
  - <sup>19</sup> Alejandro Molina-Sánchez, Davide Sangalli, Kerstin Hummer, Andrea Marini, and Ludger Wirtz, “Effect of spin-orbit interaction on the optical spectra of single-layer, double-layer, and bulk MoS<sub>2</sub>,” *Phys. Rev. B* **88**, 045412 (2013).
  - <sup>20</sup> Alejandro Molina-Sánchez, Maurizia Palummo, Andrea Marini, and Ludger Wirtz, “Temperature-dependent excitonic effects in the optical properties of single-layer MoS<sub>2</sub>,” *Phys. Rev. B* **93**, 155435 (2016).
  - <sup>21</sup> Aaron M. Jones, Hongyi Yu, Nirmal J. Ghimire, Sanfeng Wu, Grant Aivazian, Jason S. Ross, Bo Zhao, Jiaqiang Yan, David G. Mandrus, Di Xiao, Wang Yao, and Xiaodong Xu, “Optical generation of excitonic valley coherence in monolayer WSe<sub>2</sub>,” *Nature Nanotechnology* **8**, 634 EP – (2013).
  - <sup>22</sup> Di Xiao, Gui-Bin Liu, Wanxiang Feng, Xiaodong Xu, and Wang Yao, “Coupled Spin and Valley Physics in Monolayers of MoS<sub>2</sub> and Other Group-VI Dichalcogenides,” *Phys. Rev. Lett.* **108**, 196802 (2012).
  - <sup>23</sup> Kin Fai Mak, Keliang He, Jie Shan, and Tony F. Heinz, “Control of valley polarization in monolayer MoS<sub>2</sub> by optical helicity,” *Nature Nanotechnology* **7**, 494 EP – (2012).
  - <sup>24</sup> Hiram J. Conley, Bin Wang, Jed I. Ziegler, Richard F. Haglund, Sokrates T. Pantelides, and Kirill I. Bolotin, “Bandgap Engineering of Strained Monolayer and Bilayer MoS<sub>2</sub>,” *Nano Letters* **13**, 3626–3630 (2013).
  - <sup>25</sup> Yumeng You, Xiao-Xiao Zhang, Timothy C. Berkelbach, Mark S. Hybertsen, David R. Reichman, and Tony F. Heinz, “Observation of biexcitons in monolayer WSe<sub>2</sub>,” *Nature Physics* **11**, 477 EP – (2015).
  - <sup>26</sup> Meinrad Sidler, Patrick Back, Ovidiu Cotlet, Ajit Srivastava, Thomas Fink, Martin Kroner, Eugene Demler, and Atac Imamoglu, “Fermi polaron-polaritons in charge-tunable atomically thin semiconductors,” *Nature Physics* **13**, 255 EP – (2016).
  - <sup>27</sup> Kin Fai Mak, Keliang He, Changgu Lee, Gwan Hyoun Lee, James Hone, Tony F. Heinz, and Jie Shan, “Tightly bound trions in monolayer MoS<sub>2</sub>,” *Nature Materials* **12**, 207 EP – (2012).
  - <sup>28</sup> Ke Wang, Kristiaan De Greve, Luis A. Jauregui, Andrey Sushko, Alexander High, You Zhou, Giovanni Scuri, Takashi Taniguchi, Kenji Watanabe, Mikhail D. Lukin, Hongkun Park, and Philip Kim, “Electrical control of charged carriers and excitons in atomically thin materials,” *Nature Nanotechnology* **13**, 128–132 (2018).
  - <sup>29</sup> Carmen Palacios-Berraquero, Dhiren M. Kara, Alejandro R. P. Montblanch, Matteo Barbone, Pawel Latawiec,

- Duhee Yoon, Anna K. Ott, Marko Loncar, Andrea C. Ferrari, and Mete Atatüre, “Large-scale quantum-emitter arrays in atomically thin semiconductors,” *Nature Communications* **8**, 15093 EP – (2017), article.
- <sup>30</sup> R. F. Frindt, “Optical Absorption of a Few Unit-Cell Layers of MoS<sub>2</sub>,” *Phys. Rev.* **140**, A536–A539 (1965).
- <sup>31</sup> Lukas Mennel, Marco M. Furchi, Stefan Wachter, Matthias Paur, Dmitry K. Polyushkin, and Thomas Mueller, “Optical imaging of strain in two-dimensional crystals,” *Nature Communications* **9**, 516 (2018).
- <sup>32</sup> Jinhua Hong, Zhixin Hu, Matt Probert, Kun Li, Danhui Lv, Xinan Yang, Lin Gu, Nannan Mao, Qingliang Feng, Liming Xie, Jin Zhang, Dianzhong Wu, Zhiyong Zhang, Chuanhong Jin, Wei Ji, Xixiang Zhang, Jun Yuan, and Ze Zhang, “Exploring atomic defects in molybdenum disulphide monolayers,” *Nature Communications* **6**, 6293 EP – (2015), article.
- <sup>33</sup> Haining Wang, Changjian Zhang, and Farhan Rana, “Ultrafast Dynamics of Defect-Assisted Electron-Hole Recombination in Monolayer MoS<sub>2</sub>,” *Nano Letters* **15**, 339–345 (2015).
- <sup>34</sup> Jiamin Xue, Javier Sanchez-Yamagishi, Danny Bulmash, Philippe Jacquod, Aparna Deshpande, K. Watanabe, T. Taniguchi, Pablo Jarillo-Herrero, and Brian J. LeRoy, “Scanning tunnelling microscopy and spectroscopy of ultra-flat graphene on hexagonal boron nitride,” *Nature Materials* **10**, 282 EP – (2011).
- <sup>35</sup> Raphael Brechbühler, Freddy T. Rabouw, Patrik Rohner, Boris le Feber, Dimos Poulikakos, and David J. Norris, “Two-Dimensional Drexhage Experiment for Electric- and Magnetic-Dipole Sources on Plasmonic Interfaces,” *Phys. Rev. Lett.* **121**, 113601 (2018).
- <sup>36</sup> Lutz Langguth, Romain Fleury, Andrea Alù, and A. Femius Koenderink, “Drexhage’s Experiment for Sound,” *Phys. Rev. Lett.* **116**, 224301 (2016).
- <sup>37</sup> Haining Wang, Changjian Zhang, Weimin Chan, Christina Manolatu, Sandip Tiwari, and Farhan Rana, “Radiative lifetimes of excitons and trions in monolayers of the metal dichalcogenide MoS<sub>2</sub>,” *Phys. Rev. B* **93**, 045407 (2016).
- <sup>38</sup> Daniel B. S. Soh, Christopher Rogers, Dodd J. Gray, Eric Chatterjee, and Hideo Mabuchi, “Optical nonlinearities of excitons in monolayer MoS<sub>2</sub>,” *Phys. Rev. B* **97**, 165111 (2018).
- <sup>39</sup> Yifei Yu, Chun Li, Yi Liu, Liqin Su, Yong Zhang, and Linyou Cao, “Controlled Scalable Synthesis of Uniform, High-Quality Monolayer and Few-layer MoS<sub>2</sub> Films,” *Scientific Reports* **3**, 1866 EP – (2013), article.
- <sup>40</sup> YiHsien Lee, XinQuan Zhang, Wenjing Zhang, MuTung Chang, ChengTe Lin, KaiDi Chang, YaChu Yu, Jacob TseWei Wang, ChiaSeng Chang, LainJong Li, and TsungWu Lin, “Synthesis of LargeArea MoS<sub>2</sub> Atomic Layers with Chemical Vapor Deposition,” *Advanced Materials* **24**, 2320–2325.
- <sup>41</sup> Christopher Rogers, Dodd Gray, Nate Bogdanowicz, and Hideo Mabuchi, “Laser annealing for radiatively broadened MoSe<sub>2</sub> grown by chemical vapor deposition,” *Phys. Rev. Materials* **2**, 094003 (2018).
- <sup>42</sup> P. J. Zomer, M. H. D. Guimares, J. C. Brant, N. Tombros, and B. J. van Wees, “Fast pick up technique for high quality heterostructures of bilayer graphene and hexagonal boron nitride,” *Applied Physics Letters* **105**, 013101 (2014).
- <sup>43</sup> Filippo Pizzocchero, Lene Gammelgaard, Bjarke S. Jessen, José M. Caridad, Lei Wang, James Hone, Peter Bøggild, and Timothy J. Booth, “The hot pick-up technique for batch assembly of van der Waals heterostructures,” *Nature Communications* **7**, 11894 EP – (2016), article.
- <sup>44</sup> F. Wooten, *Optical properties of solids* (Academic Press, 1972) Chap. 3.
- <sup>45</sup> Charalambos C. Katsidis and Dimitrios I. Siapkas, “General transfer-matrix method for optical multilayer systems with coherent, partially coherent, and incoherent interference,” *Appl. Opt.* **41**, 3978–3987 (2002).
- <sup>46</sup> Yuyan Liu, Jieli Lin, Guangming Huang, Yuanqing Guo, and Chuanxi Duan, “Simple empirical analytical approximation to the Voigt profile,” *J. Opt. Soc. Am. B* **18**, 666–672 (2001).
- <sup>47</sup> J.J. Olivero and R.L. Longbothum, “Empirical fits to the Voigt line width: A brief review,” *Journal of Quantitative Spectroscopy and Radiative Transfer* **17**, 233 – 236 (1977).
- <sup>48</sup> You Zhou, Giovanni Scuri, Jiho Sung, Ryan J. Gelly, Dominik S. Wild, Kristiaan De Greve, Andrew Y. Joe, Takashi Taniguchi, Kenji Watanabe, Philip Kim, Mikhail D. Lukin, and Hongkun Park, “Controlling excitons in an atomically thin membrane with a mirror,” arXiv e-prints, arXiv:1901.08500 (2019), [arXiv:1901.08500 \[cond-mat.mes-hall\]](https://arxiv.org/abs/1901.08500).
- <sup>49</sup> Nate Bogdanowicz, Christopher Rogers, Dodd Gray, Chris Timossi, Francesco Marazzi, Jonathan Wheeler, and Ivan Galinskiy, “mabuchilab/Instrumental: 0.5,” (2018), [10.5281/zenodo.2556399](https://zenodo.org/record/2556399).



## II. ADDITIONAL INFORMATION

Supplementary Information is linked to the online version of the paper.

## ACKNOWLEDGMENTS

This work was funded in part by the National Science Foundation (NSF) awards PHY-1648807 and DMR-1838497, and also by a seed grant from the Precourt Institute for Energy at Stanford University. Part of this work was performed at the Stanford Nano Shared Facilities (SNSF), supported by the NSF under award ECCS-1542152. C.R., D.G., and N.B. were supported in part by Stanford Graduate Fellowships. C.R. was also supported in part by a Natural Sciences and Engineering Research Council of Canada doctoral postgraduate scholarship. K.W. and T.T. acknowledge support from the Elemental Strategy Initiative conducted by the MEXT, Japan and the CREST (JPMJCR15F3), JST. All authors thank Tatsuhiko Onodera for discussions relating to the reflectance model. All authors thank Daniel B. S. Soh and Eric Chatterjee for discussions relating to exciton physics. C.R. thanks Joe Finney, Giovanni Scuri and Elyse Barre for help with heterostructure fabrica-

tion, Logan Wright for pointing out relevant literature, and Peter L. McMahon for suggestions relating to the manuscript.

## III. AUTHOR CONTRIBUTIONS

C.R. conceived the experiments, fabricated the samples, performed the experiments, and performed the data analysis. C.R. and D.G. built the confocal microscope setup for the cryostat, as well as the grating spectrometer. C.R. and N.B. automated the measurements. T.T. and K.W. grew the hBN. C.R., N.B., D.G. and H.M. all contributed to the manuscript.

## IV. COMPETING FINANCIAL INTEREST

The authors declare no competing financial interests.

## V. DATA AVAILABILITY

The data that support the findings of this study are available from the corresponding author upon reasonable request.

# Coherent Control of Two-Dimensional Excitons

## Supplemental Methods

Christopher Rogers,<sup>1,\*</sup> Dodd Gray, Jr.,<sup>1</sup> Nathan Bogdanowicz,<sup>1</sup>

Takashi Taniguchi,<sup>2</sup> Kenji Watanabe,<sup>2</sup> and Hideo Mabuchi<sup>1,†</sup>

<sup>1</sup>*Ginzton Laboratory, Stanford University,*

*348 Via Pueblo, Stanford, CA 94305*

<sup>2</sup>*National Institute for Materials Science,*

*1-1 Namiki, Tsukuba 305-0044, Japan*

(Dated: December 29, 2021)

---

\* cmrogers@stanford.edu

† hmabuchi@stanford.edu

## I. SUPPLEMENTAL METHODS

### A. Sample Fabrication

We fabricate heterostructures using a dry pickup transfer technique [42, 43]. We first clean 300 nm  $\text{SiO}_2$  on Si substrates, and fused silica substrates by sonicating in acetone for 2 minutes, then deionized water for 2 minutes and finally isopropanol for 2 minutes. The substrates are then subjected to oxygen plasma for 5 minutes. Graphite (NGS Naturegraphit GmbH), hexagonal Boron Nitride (hBN), and  $\text{MoSe}_2$  (2D Semiconductors or HQ Graphene) are then exfoliated onto the freshly cleaned substrates using Scotch tape. The substrates are observed under an optical microscope to identify monolayer  $\text{MoSe}_2$ , few-layer graphene and 50-120 nm hBN.

Polydimethylsiloxane (PDMS) with thin polycarbonate (PC) stamps are used to create the heterostructures. To produce the stamp, a 6% PC solution is used to form a thin film on a glass slide. This thin film is then transferred onto a 1 mm  $\times$  1 mm piece of PDMS on a different glass slide using Scotch tape with a hole punched in the middle. This stamp is then used to sequentially pick up the mechanically exfoliated flakes by bringing the stamp slowly into contact with a flake on the exfoliation substrate. In our case, we first pick up the ‘top’ hBN, then the monolayer  $\text{MoSe}_2$ , then the ‘bottom’ hBN, and finally the few-layer graphene flake. Each flake is picked up at a temperature of about 60 °C. This stack (including the PC film) is transferred to a glass substrate by heating the substrate to 140 °C and bringing the stamp into contact. After letting the sample sit for one day, the PC is removed by dissolution in chloroform.

## B. Experimental Setup

A detailed experimental schematic is shown in Fig. S1. The experiment is conducted in an optical cryostat (Montana Instruments Nanoscale Workstation) at a nominal temperature of 4 K and a pressure of  $1 \cdot 10^{-7}$  Torr. The sample is attached to a fixed mount while the gold mirror is actuated by a slip-stick piezo mirror mount (Janssen Precision Engineering).

Light from either a lamp (Thorlabs SLS201) or a supercontinuum laser (NKT Photonics SuperK) is coupled into the custom confocal microscope through a single mode optical fiber. Two reflective collimators serve to couple the microscope to the single mode fibers for excitation and reflection. The excitation and reflection paths are separated by a 50/50 non-polarizing beamsplitter. Two achromatic lenses with focal length  $f_1 = 75\text{mm}$  form the first 4f system. The first of these lenses is translated along the optical axis using a motorized stage, which shifts the focus of the beam at the sample along the optical axis. The range of travel of the beam focus at the sample is approximately  $\pm 200\text{ }\mu\text{m}$ . A tip-tilt mirror mechanically actuated by motorized stages (Newport U100-A and Newport LTA-HS) at the beginning of the second 4f section (comprised of two achromatic lenses of focal length  $f_2 = 150\text{ mm}$ ) shifts the beam in the transverse plane at the sample. The total travel of the beam focus is about  $\pm 300\text{ }\mu\text{m}$ . A microscope objective ( $20\times$ , 0.4 numerical aperture, Olympus MSPLAN) inside the optical cryostat focuses the light down on the sample and mirror. Light is collected back through the same optical path, and sent to a grating spectrometer for measurement. A removable beamsplitter enables imaging of the sample. Note that the lens imaging onto the camera in the imaging train is also on a translation stage, allowing the imaging plane to be matched with that of the excitation spot.

The grating spectrometer used to measure the reflectance spectra has an 1800 line/mm



reflective diffraction grating on a motorized rotation stage (Newport RGV100). Spectra are measured using a camera (Princeton Instruments PIXIS 2048). The nominal resolution of the spectrometer is approximately  $1 \text{ cm}^{-1}$ .

### C. Reflectance Model Fitting

We simultaneously fit spectral data in Figs. 2a and 2c from several selected characteristic  $z$  positions to the full reflectance model in Eq. 3. The absolute value of the discrepancy between the reflectance model and the experimental data over the selected  $z$  values was simultaneously minimized to find the global fitting parameters  $\omega_0 = 1647.72 \text{ meV}$ ,  $\gamma_{r,0} = 1.09 \text{ meV}$ ,  $\gamma_{nr} = 0.40 \text{ meV}$  and  $\gamma_{ib} = 0.26 \text{ meV}$ . The experimental spectra selected for the fitting procedure and the corresponding modeled reflectance given by the optimized fitting parameters are shown in Fig. S2.

We note that the four fitting parameters are highly constrained by the experimental data, and that other values of the parameters do not produce satisfactory agreement between experiment and model. For simplicity we ignore the subtle difference between  $\gamma_{ib}$  and  $\gamma_{ib,\text{eff}}$ . Doing so does not qualitatively alter the conclusions reached. First,  $\omega_0$  is set by the position of the reflectance dip at both  $z_c$  and  $z_{d,1/2}$ . Second, the quantity  $\gamma_{nr} + \gamma_{ib}$  is constrained by the reflectance linewidth at  $z_d$ , where radiative broadening is negligible. Similarly, the total linewidth  $\gamma_{\text{tot}} = \gamma_r + \gamma_{nr} + \gamma_{ib}$  is constrained by the linewidth at  $z_c$ . Lastly, the magnitude of the on-resonant reflection at  $z_c$  constrains the ratio  $\gamma_r/(\gamma_{nr} + \gamma_{ib})$ . Because the modulation of  $\gamma_r$  by the mirror is independent of the fitting parameters, we can conceptually replace  $\gamma_r$  in the above discussion by  $A\gamma_{r,0}$  (where  $A$  is constant). The four independent relations above then fully constrain the fitting parameters.

The static (unfitted) parameters used in the reflectance model are as follows. The index

of the silica substrate is  $n = 1.45$ , and the index of the hBN is  $n = 1.9$ . The index of refraction of the gold at  $\omega_0$  is  $n = 0.1388 + 4.4909i$ . The thickness of the gold is 120 nm. The thickness of the top hBN is 87 nm, and the thickness of the bottom hBN is 128 nm. The background index of the MoSe<sub>2</sub> is  $n = 4.5$ . The graphene flake is modeled as a bilayer with an index at  $\omega_0$  of  $n = 2.15 + 1.91i$ .

#### D. Mirror Position Fitting

The slip-stick piezo stage used to actuate the mirror does not have any position encoding, which requires us to have an independent measure of the mirror position. At each  $z$  position for the data in Figs. 2a and 2c, we also took spectra over the range of 770 nm to 900 nm from the same position on the sample. As can be seen in Fig. S3, there are broad fringes that vary with mirror position, due primarily to the modulation of absorption in the gold mirror and the few-layer graphene as the mirror position is changed. Treating  $z$  as a free parameter, we fit the reflectance in this region to the same reflectance model for the full heterostructure shown in Eq. 3. Note that because these spectra are off-resonant from  $X_0$ , the exciton susceptibility has a negligible effect. Several examples of the measured and fitted spectra are shown in Fig. S3.

#### E. Linewidth Model

From [5], for an ideal dipole near and parallel to an ideal mirror:

$$\frac{\tau_x}{\tau_0} = \left[ 1 - \frac{3 \sin x}{2x} - \frac{3 \cos x}{2x^2} + \frac{3 \sin x}{2x} \right]^{-1} \quad (\text{S1})$$

where  $\tau_x$  is the lifetime at normalized distance  $x = \frac{4\pi z}{\lambda_0}$  from the mirror,  $\tau_0$  is the lifetime in vacuum,  $\lambda_0$  is the wavelength in vacuum and  $z$  is the *optical* path length between the

mirror and the dipole. When the dipole has a coherent quantum efficiency  $\eta_0$  in vacuum, the modified lifetime  $\tau'_x$  is:

$$\frac{\tau'_x}{\tau_0} = \frac{1}{1 + \eta_0 \left( \frac{\tau_0}{\tau_x} - 1 \right)} \quad (\text{S2})$$

It then follows from Eq. S1 that the radiative decay rate  $\gamma_r$  for a perfect dipole is:

$$\frac{\gamma_r}{\gamma_{r,0}} = 1 - \frac{3 \sin x}{2x} - \frac{3 \cos x}{2x^2} + \frac{3 \sin x}{2x^3} \quad (\text{S3})$$

where  $\gamma_{r,0}$  is the radiative decay rate in vacuum. For the more general case with sub-unity coherent quantum efficiency  $\eta_0 = \frac{\gamma_{r,0}}{\gamma_{\text{tot},0}}$ , with  $\gamma_{\text{tot},0}$  being the total linewidth in vacuum, it follows from Eq. S2 that:

$$\frac{\gamma_{\text{tot}}(x)}{\gamma_{\text{tot},0}} = 1 + \eta_0 \left( \frac{\gamma_r}{\gamma_{r,0}} - 1 \right) \quad (\text{S4})$$

Using Eq. S3 we find that:

$$\frac{\gamma_{\text{tot}}(x)}{\gamma_{\text{tot},0}} = 1 + \eta_0 \left[ \frac{3 \sin x}{2x^3} - \frac{3 \cos x}{2x^2} - \frac{3 \sin x}{2x} \right] \quad (\text{S5})$$

For a 2D dipole the case is different. Assuming that the dipole has perfect transverse coherence and thus emits only into forward and backward plane wave modes, the modification of  $\gamma_r$  is determined by the interference between  $-e^{ik_0 d_{\text{opl}}}$  and 1. Here  $k = \frac{2\pi}{\lambda_0}$  is the wavenumber of the light in vacuum and  $d_{\text{opl}}$  is the total *optical* path length traversed by the backwards-emitted wave until it comes back to the 2D dipole. The negative sign comes from the phase flip on reflection. Thus, we can write down the modification of radiative decay rate:

$$\frac{\gamma_r}{\gamma_{r,0}} = \text{Re} [1 - e^{ik_0 d_{\text{opl}}}] = 1 - \cos(k_0 d_{\text{opl}}) \quad (\text{S6})$$

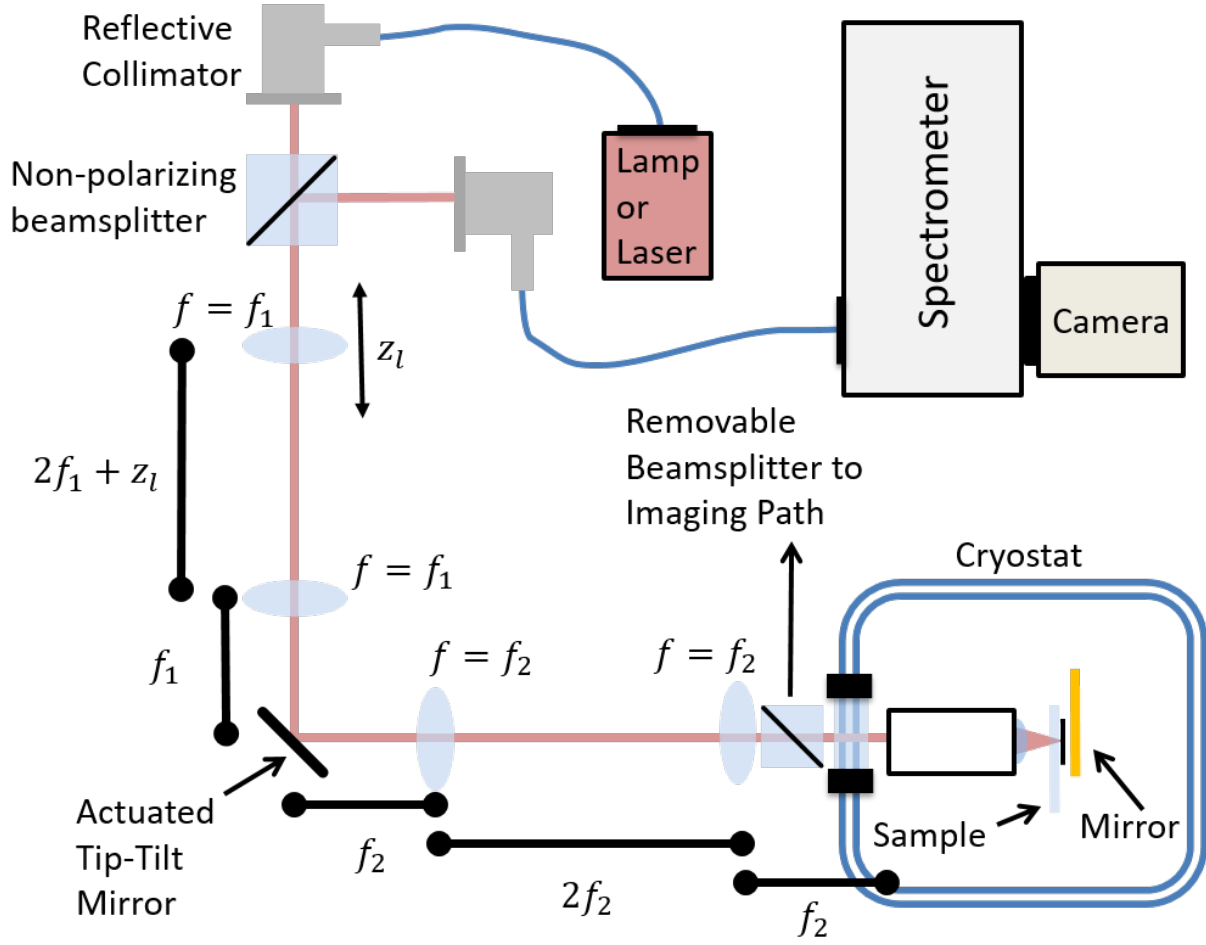
Identifying that  $d_{\text{opl}} = 2z$ :

$$\frac{\gamma_r}{\gamma_{r,0}} = 1 - \cos(2k_0 z) = 1 - \cos(x) \quad (\text{S7})$$

Using Eq. S4, which holds for a 2D dipole as well, we find that:

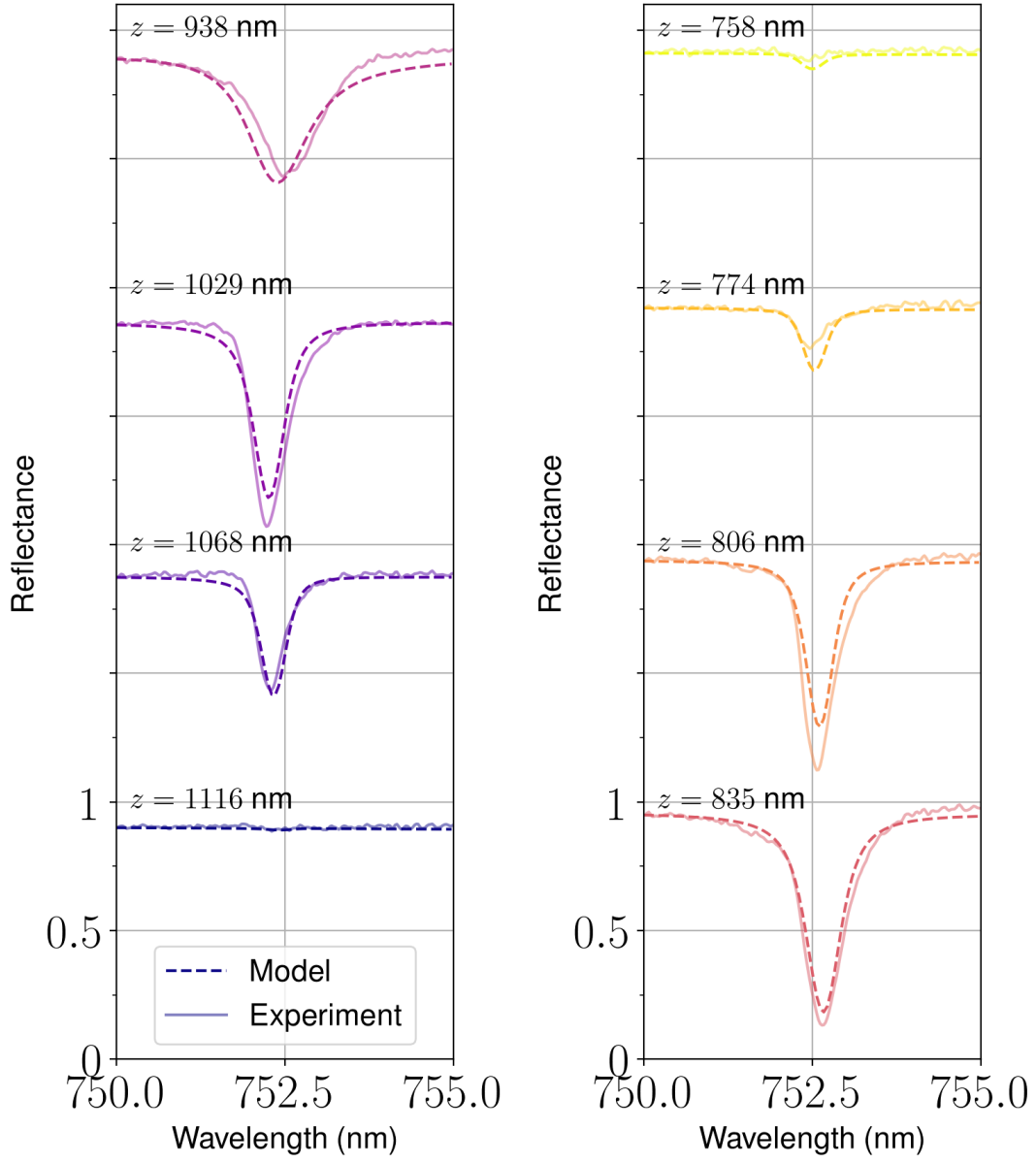
$$\frac{\gamma_{\text{tot}}(x)}{\gamma_{\text{tot},0}} = 1 - \eta_0 \cos(x) \quad (\text{S8})$$





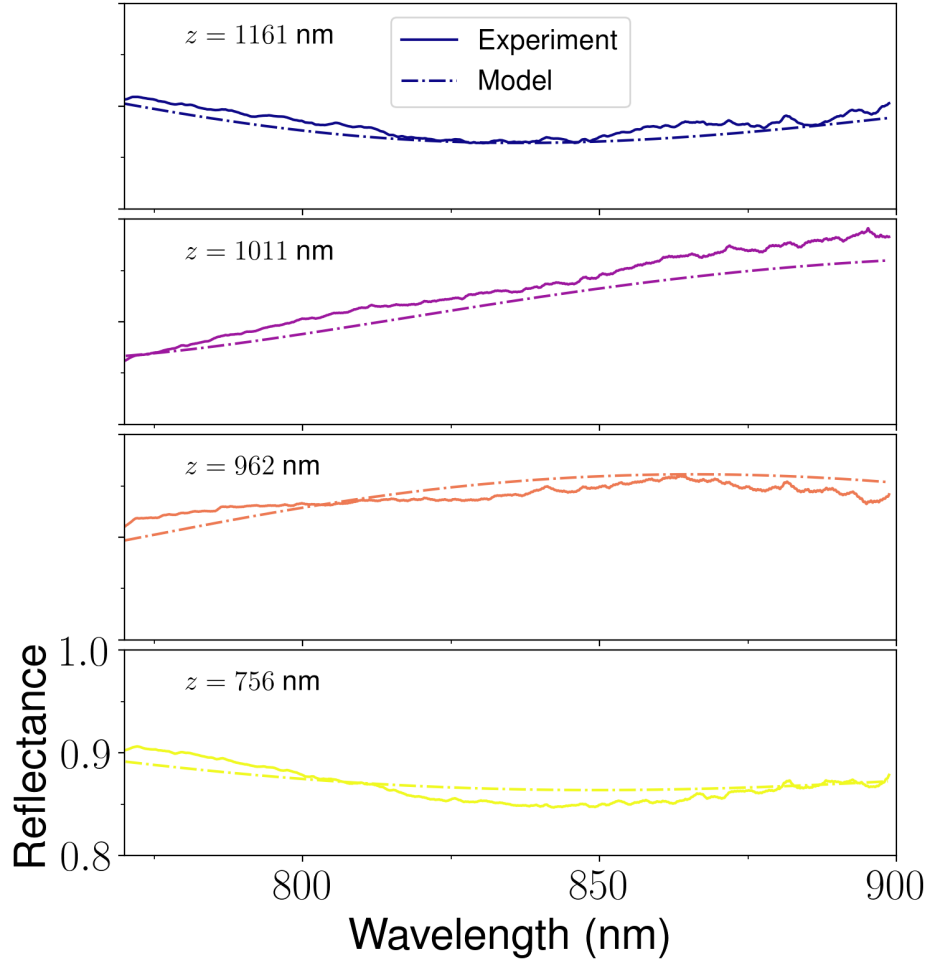
(a)

**FIG. S1. Experimental Setup.** Light is coupled from a lamp or a laser through a single mode fiber into a custom confocal microscope, which focuses light on the sample and collects the reflection. The collected light is measured using a grating spectrometer.



(a)

FIG. S2. **Characteristic spectra used to fit the model parameters.** The experimental data is shown in solid lines, and the model in dashed lines. The mirror position  $z$  corresponding to each spectrum is shown.



(a)

FIG. S3. **Selected spectra used to extract the mirror position  $z$ .** Data from the experiment is shown with solid lines, and the model is shown with dashed lines. The mirror position  $z$  corresponding to each spectrum is labeled.